

# Boosting silica micro-rod $Q$ factor to $8.28 \times 10^9$ for fully stabilizing a soliton microcomb

Received: 29 January 2025

Accepted: 28 August 2025

Published online: 06 October 2025



Ting-Yang Pan<sup>1,2,6</sup>, Teng Tan<sup>3,4,6</sup>, Bing Duan<sup>1,2,6</sup>, Bing Chang<sup>3,6</sup>, Fan Tang<sup>3</sup>, Yong-Jun Huang<sup>3</sup>, Ying-Zhan Yan<sup>5</sup>, Shan-Guo Huang<sup>1</sup>✉, Da-Quan Yang<sup>1,2</sup>✉ & Bai-Cheng Yao<sup>3</sup>✉

Optical microcavities with strong light confinement are powerful tools for significantly enhancing light-matter interactions. Currently, the actual  $Q$  factor of a microcavity remains far below the theoretical limit, as specific factors affecting losses inside microcavities are not yet fully quantified. Here, using silica whispering-gallery-mode microrod cavities, we quantitatively identify how radiation loss, scattering loss, and contaminant loss contribute to the total loss, finding that after fine fabrication, contaminant loss is the major factor limiting the total cavity  $Q$ . By employing two-step laser polishing and heat treatment, we achieve a  $Q$  factor of up to  $8.28 \times 10^9$ . Accordingly, we demonstrate a fully stabilized soliton microcomb system using the  $Q$ -enhanced microcavity, achieving phase noise suppression of over 45.2 dB at the pump frequency and over 60.6 dB at the repetition frequency. This work deepens the understanding of intracavity loss and may pave the way for practically improving the performance of microcavity photonics.

Optical microcavities, which typically exhibit high-quality ( $Q$ ) factors, are capable of confining light fields in both spatial and temporal dimensions<sup>1–3</sup>. This property significantly enhances light-matter interactions, making them a crucial platform for various applications ranging from optical physics<sup>4–6</sup> to integrated photonic devices<sup>7–12</sup>. In a microcavity, the  $Q$  factor is a crucial physical parameter. A higher  $Q$  factor indicates an enhanced ability to extend photon lifetimes, increase intracavity light field energy, and reduce nonlinear thresholds. As a result, continuous efforts have been dedicated to refining micro-fabrication processes across different material platforms to boost the  $Q$  factor of microcavities and thereby enhance the performance of microcavity-based photonic devices. Notable advancements in increasing the  $Q$  factor have been achieved on platforms using materials such as thermal silica<sup>13–15</sup>,  $\text{Si}_3\text{N}_4$ <sup>16,17</sup>,  $\text{SiC}$ <sup>18,19</sup>,  $\text{AlN}$ <sup>20,21</sup>,  $\text{LiNbO}_3$ <sup>22,23</sup>, and  $\text{MgF}_2/\text{CaF}_2$ <sup>24,25</sup>. These enhancements have enabled critical applications, including miniature optical frequency combs<sup>26–29</sup>, high-coherence

lasers<sup>30,31</sup>, high-speed optical communications<sup>32–34</sup>, LiDAR<sup>35,36</sup>, sensing<sup>37–41</sup>, and optical gyroscopes<sup>42–44</sup>.

Fundamentally, the intrinsic  $Q$  factor ( $Q_0$ ), associated with all the losses in an optical microcavity, determines the oscillating properties. The total losses within an optical microcavity include absorption loss, radiation & scattering loss, and contaminant loss. To increase the intrinsic  $Q$  factor, various strategies have been explored to mitigate these losses. For example, radiation, scattering, and absorption losses can be reduced by increasing the size of a microresonator<sup>45</sup>, smoothing the interfaces<sup>46,47</sup>, and selecting appropriate cavity materials<sup>48</sup>. However, limited research has been conducted to quantitatively analyze the specific loss factors that individually impact the  $Q_0$  factor of a microcavity; this is a key reason that it is hard for scientists to bridge the gap between actual and theoretical  $Q_0$  values. For example, due to its high preparation convenience, structural flexibility, low cost, and system

<sup>1</sup>State Key Laboratory of Information Photonics and Optical Communications, Beijing University of Posts and Telecommunications, Beijing, China. <sup>2</sup>School of Information and Communication Engineering, Beijing University of Posts and Telecommunications, Beijing, China. <sup>3</sup>Key Laboratory of Optical Fiber Sensing and Communications (Education Ministry of China), University of Electronic Science and Technology of China, Chengdu, China. <sup>4</sup>Institute of Electronic and Information Engineering of UESTC, Guangdong, China. <sup>5</sup>National Key Laboratory of Integrated Circuits and Microsystems, China Electronics Technology Group Corporation, Beijing, China. <sup>6</sup>These authors contributed equally: Ting-Yang Pan, Teng Tan, Bing Duan, Bing Chang. ✉e-mail: [shghuang@bupt.edu.cn](mailto:shghuang@bupt.edu.cn); [ydq@bupt.edu.cn](mailto:ydq@bupt.edu.cn); [yaobaicheng@uestc.edu.cn](mailto:yaobaicheng@uestc.edu.cn)

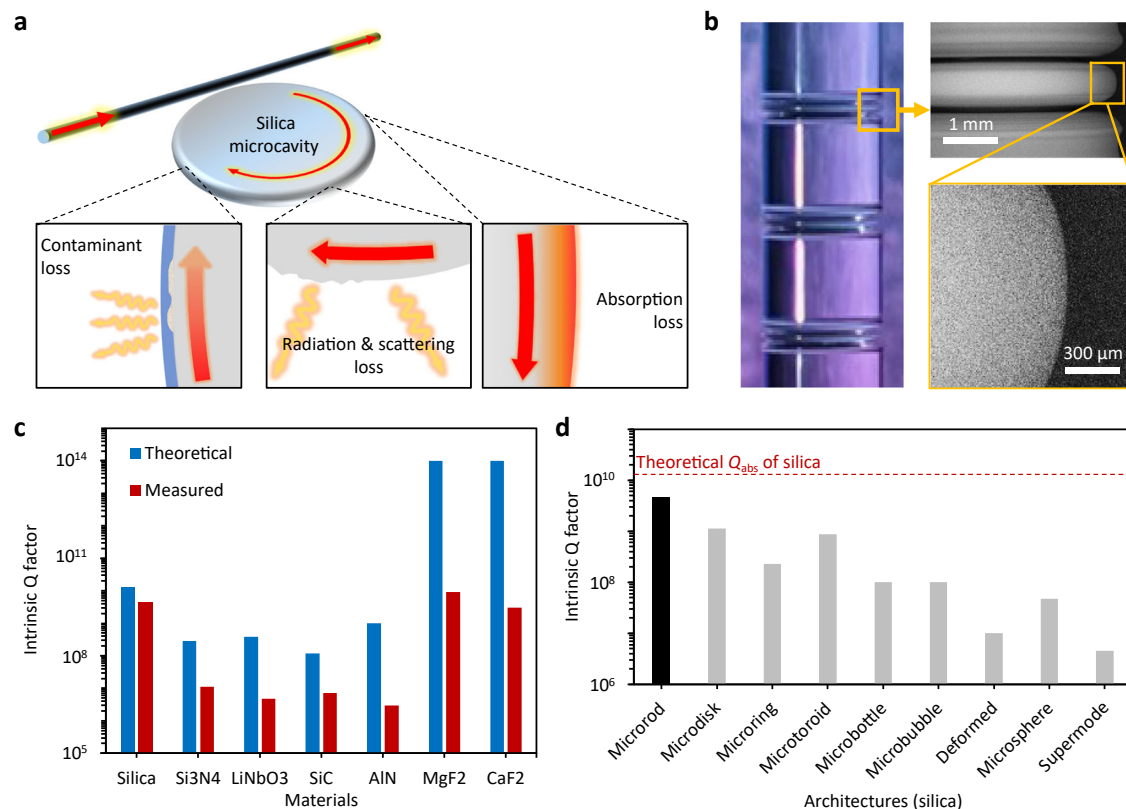


**Fig. 1 | Losses in a microresonator and typical intrinsic  $Q$  factors. a** Illustration of the losses in a microcavity, including radiation & scattering loss, material absorption loss and contaminant loss. **b** Images of our fused silica microrod cavity, embedded within the 3-mm-diameter fiber preform. Here we also show the

scanning electron microscope (SEM) images of microrod resonator. **c** Theoretical and measured  $Q_0$  of state-of-the-art microcavities in diverse material platform. **d** Measured  $Q_0$  of different silica microcavities.

compatibility, silica whispering-gallery-mode (WGM) microcavity is one of the most widely used architectures<sup>5,13,14,49–52</sup>. However, compared to a standard silica fiber (total loss at the level of  $10^{-4}$  dB/m), the current loss of a WGM microcavity is on the order of  $10^{-2}$  dB/m, and this results in its  $Q_0$  typically being lower than  $10^9$ <sup>13</sup>, which is far from reaching the theoretical limit of around  $10^{10}$ . A major reason for this fact is the challenges in quantitative characterization and effective suppression of the contaminant loss in a silica WGM microcavity.

In this study, we comprehensively examine the impact of specific loss factors on the  $Q_0$  of a microcavity and present a method to enhance the intrinsic  $Q$  factor of a silica micro-rod to  $8.28 \times 10^9$ , approaching the theoretical limit. By separately characterizing losses induced by radiation, scattering, and material absorption, we accurately determine the value of contaminant loss, which was hard to measure directly. We identify that contaminant loss predominantly hinders the increase of the  $Q_0$  factor in a high-quality silica WGM microcavity, both in theory and in experiment. This demonstrates that effectively removing surface contamination is a prerequisite for achieving an impressive  $Q_0$  factor. In a standard silica microrod cavity, we quantitatively demonstrate that losses due to radiation/scattering, absorption, and contaminants are  $2.41 \times 10^{-8}$ ,  $7.94 \times 10^{-11}$ , and  $8.68 \times 10^{-10}$ , respectively. Then, we develop a laser-smoothing technique to suppress radiation/scattering losses and devise a method to remove contaminants. After these optimizations, the radiation/scattering loss and contaminant loss in our microcavity are reduced to  $4.5 \times 10^{-12}$  and  $3.67 \times 10^{-11}$ , leading to a world-class  $Q_0$  of  $8.28 \times 10^9$ . Moreover, utilizing this high- $Q$  microcavity as a frequency reference, we demonstrate its unique capability to fully stabilize a soliton microcomb in a practically compact size. Our results showcase a phase noise suppression of more

than 45.2 dB for the pump laser and over 60.6 dB for the repetition rate.

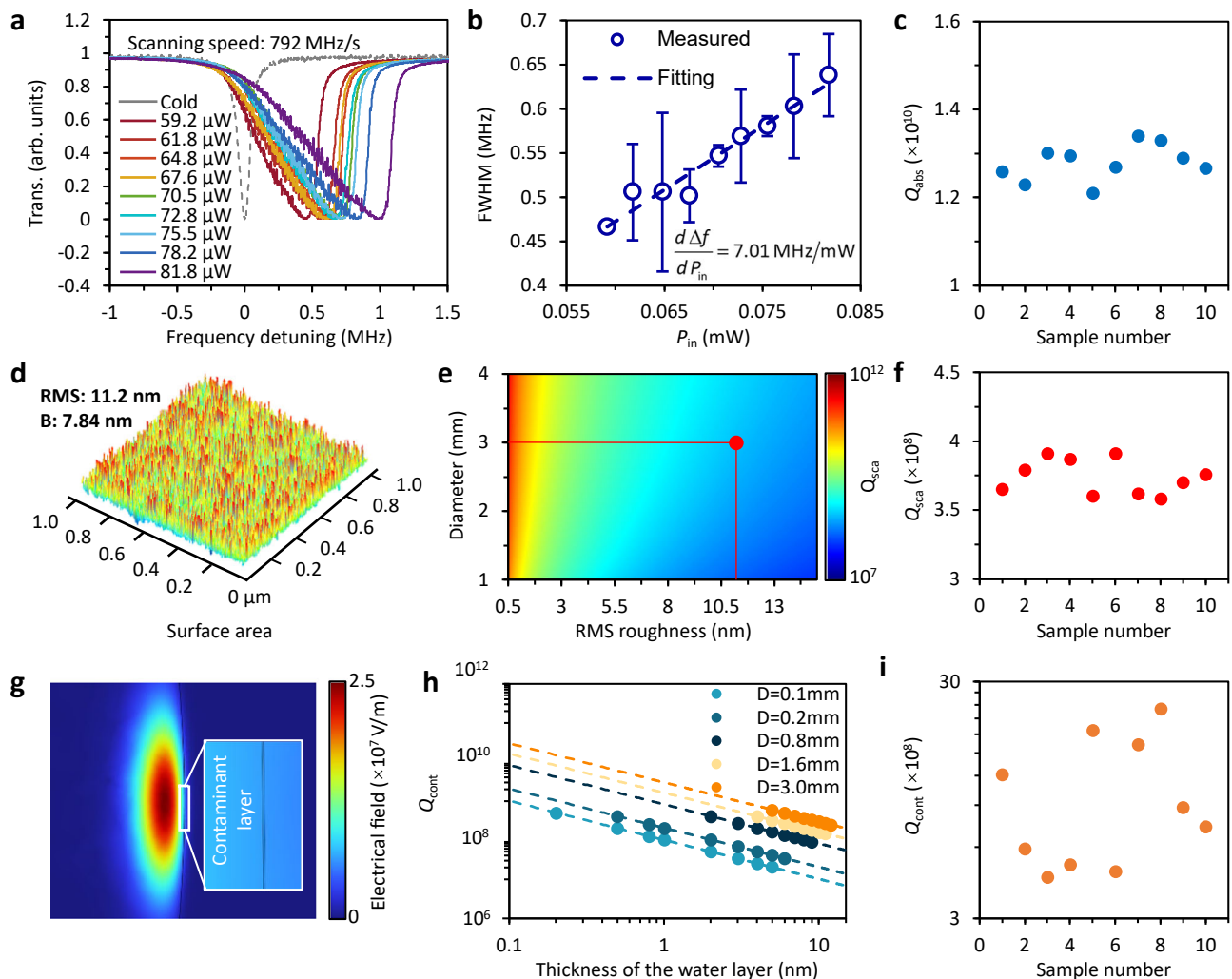
## Results

Figure 1a illustrates the conceptual architecture of a microcavity and highlights the sources of intracavity losses. Typically, there are 3 types of losses in a silica microcavity that determine the  $Q_0$ :

$$Q_0^{-1} = Q_{\text{rad\&sca}}^{-1} + Q_{\text{abs}}^{-1} + Q_{\text{cont}}^{-1} \quad (1)$$

Here,  $1/Q_{\text{rad\&sca}}$  represents scattering losses due to intrinsic radiation and residual surface inhomogeneities,  $1/Q_{\text{abs}}$  accounts for absorption loss related to the material, and  $1/Q_{\text{cont}}$  corresponds to contaminant loss caused by surface contaminants. Previous studies have focused extensively on  $1/Q_{\text{rad\&sca}}$  and  $1/Q_{\text{abs}}$ . However, in the context of whispering-gallery mode (WGM) microresonators,  $1/Q_{\text{cont}}$  is crucial but has not received adequate attention, as it is hard to measure directly. In this study, to quantify all these losses in a WGM microcavity, we first prepare a silica microrod resonator, as the platform for experimental test (Fig. 1b). Using a laser-machining process<sup>49,53,54</sup>, we create a rotationally symmetric protrusion around the fused silica fiber preform (see Supplementary Note S2.1). The diameter of the microrod cavity is 3.0 mm, corresponding to a free spectral range (FSR) of 22 GHz. We also present its scanning electron microscope (SEM) image in this figure.

In Fig. 1c, we review the intrinsic  $Q$  factors of advanced microcavity material platforms<sup>19,24,25,49,55–57</sup>, referencing the theoretical  $Q_0$  factor limitation (determined by absorption):  $Q_{\text{abs}} = (4343/\alpha_{\text{abs}}) \times (2\pi n/\lambda_0)$ <sup>48</sup>. Here,  $\alpha_{\text{abs}}$  represents the absorption loss,  $n$  is the refractive index of the



**Fig. 2 | Qualitative and quantitative identifications of the intracavity losses.**

**a** Normalized transmission of different input power with the same scan speed 792 MHz/s, showcasing the absorption-based thermal broadening. **b** Linear fitting of the triangle's full width at half maximum (FWHM) as a function of input power  $P_{in}$ , with a fitted slope  $d\Delta f/dP_{in}$  of 7.01 MHz/mW. The vertical error bars give standard deviations in repeated measurements. **c** Measured  $Q_{abs}$  in 10 individual samples. **d** Atomic force microscope (AFM) image shows a root-mean-square

(RMS) roughness of 11.2 nm, within a surface inhomogeneity coefficient ( $B$ ) of 7.84 nm. **e** Calculated  $Q_{sca}$ , here the red dot illustrates the experimental case. **f** Measured  $Q_{sca}$  of 10 individual samples. **g** Electrical field distribution of a WGM microcavity, with diameter of 0.1 mm and a 1 nm thick water layer. **h** Calculated  $Q_{cont}$  versus thickness of water layer, in microcavities with diverse diameters. **i**  $Q_{cont}$  of 10 individual samples, which are achieved from the measured results  $1/Q_{cont} = 1/Q_0 + 1/Q_{abs} + 1/Q_{sca} + 1/Q_{rad}$ .

material, and  $\lambda_0$  is the optical wavelength. A detailed comparison with references is provided in Supplementary Table S1. Additionally, while fluorides may achieve higher theoretical  $Q_0$  values, silica remains one of the most promising material platforms for bridging the gap between actual and theoretical  $Q_0$  values. Moreover, silica microcavities offer unique advantages, such as thermal stability, dimensional flexibility, processing convenience, and low cost<sup>5,13,14,49–52</sup>, as highlighted in Supplementary Table S2. In Fig. 1d, we present both the theoretical and measured  $Q_0$  values for various state-of-the-art silica microcavities. The highest measured  $Q_0$  to date is found in microrods, reaching a value of  $4.5 \times 10^9$ , which is still less than half of the theoretical maximum<sup>49</sup>. Detailed data can be found in Supplementary Table S3.

First, in Fig. 2, we show how the various loss items are accurately identified. Through cavity-enhanced photothermal spectroscopy<sup>48</sup>, the material-limited  $Q$  factor ( $Q_{abs}$ ) can be accurately quantified (see details in Supplementary Note S1.2.1):

$$Q_{abs} = \frac{2\eta}{\kappa} \omega_0 \left( \frac{\delta f}{\delta T} C_0 \right) / \frac{d\Delta f}{dP_{in}} \quad (2)$$

In this equation,  $\eta = Q_i/Q_e$  is the coupling ratio, and  $\kappa = \kappa_0 + \kappa_{ex}$  is the total decay rate, where  $\kappa_0$  and  $\kappa_{ex}$  represent the intrinsic resonator decay rate and the coupling rate, respectively.  $\omega_0$  is the resonant frequency,  $C_0$  is the heat capacity of the microcavity,  $\delta f/\delta T$  is the resonant thermal tuning coefficient,  $\Delta f$  is the full width at half maximum (FWHM) of resonance, and  $P_{in}$  is the launched optical power. By analyzing the electric field and temperature distribution of the fundamental mode of our microrod using COMSOL simulation, we determined the heat capacity of our microcavity to be  $C_0 = 90.43$  K/W, as calculated in ref. 58 (see Supplementary Note S1.2.2), and we show more experimentally tested details about the  $Q_{abs}$  analysis in Supplementary Note S3.3.

Keeping the scan speed at 792 MHz/s, the input power is then adjusted using a variable optical attenuator (VOA), ranging from 59.2  $\mu$ W to 81.8  $\mu$ W. Figure 2a illustrates the changes in transmission trace with power adjustments, showing that higher power results in a larger FWHM. The relationship between FWHM and input power is summarized in Fig. 2b. Through linear fitting, a proportional coefficient  $d\Delta f/dP_{in}$  of 7.01 MHz/mW is obtained. By combining experimental measurements with numerical simulations (detailed in

Supplementary Note S1.2.2), all the parameters in Eq. (2) are determined, leading to a material-based loss  $\alpha_{\text{abs}} = 2.02 \text{ dB/km}$ . The corresponding material-limited  $1/Q_{\text{abs}}$  is  $7.94 \times 10^{-11}$ . Using this method, in Fig. 2c, we demonstrate the measured  $Q_{\text{abs}}$  of 10 individual microcavity samples. In average, the  $Q_{\text{abs}}$  of a silica micro-rod cavity is on the level of  $1.3 \times 10^{10}$ . It is noted that in any microresonator, improving  $1/Q_{\text{abs}}$  significantly is challenging, hence,  $Q_{\text{abs}}$  is often regarded as the theoretical maximum  $Q_0$ .

Then, we characterize the loss determined by the intracavity radiation and scattering. Here, for a silica microcavity with a diameter of up to 3.0 mm, the scattering loss is dominant. Typically, the scattering limited  $Q$  factor can be estimated as follow<sup>59</sup>:

$$Q_{\text{sca}} = \frac{\lambda_0^2 D}{2\pi^2 \sigma^2 B} \quad (3)$$

Here,  $\lambda_0$  denotes the resonant wavelength,  $D$  is the diameter,  $\sigma$  is the root-mean-square (RMS) roughness, and  $B$  is the correlation length of surface inhomogeneities. To reduce the surface roughness of the microcavity, we optimize the fabrication process. Figure 2d showcases the image measured by using atomic force microscopy (AFM). We obtain that the root-mean-square (RMS) roughness of the microresonator is 11.2 nm, with a correlation length of surface inhomogeneities  $B = 7.84 \text{ nm}$ . As  $D$  of the microcavity is 3 mm, one can get that  $1/Q_{\text{sca}}$  is  $2.69 \times 10^{-9}$ . According to Eq. (3), we calculate the  $Q_{\text{sca}}$  in Fig. 2e. In principle, by increasing microcavity diameter ( $D$ ) from 1 mm to 4 mm, while decreasing the RMS roughness from 15 nm to 0.5 nm,  $Q_{\text{sca}}$  can be boosted from  $6.9 \times 10^7$  to  $2.5 \times 10^{11}$ . In Fig. 2f, we show the measured  $Q_{\text{sca}}$  of 10 individual microcavity samples. Without further polishing, the  $Q_{\text{sca}}$  of a silica micro-rod ( $D = 3 \text{ mm}$ ) is in a range between  $3.5 \times 10^8$  and  $4 \times 10^8$ . Therefore, we note that in the common case, radiation and scattering loss is the main factor limiting the final  $Q$ .

Referring Eq. (1), now we can accurately obtain the number of  $Q_{\text{cont}}$ . In silica microcavities, typical contaminants include surface water layer<sup>60</sup> and other particulates. As illustrated in Fig. 2g, we developed a microcavity model with a water layer. The overlap areas of the mode field with the water layer can be defined as:

$$\Gamma = \frac{\int |E_{\text{water}}(x, y, z)|^2 dV}{\int |E_{\text{total}}(x, y, z)|^2 dV} \quad (4)$$

Meanwhile, we define the effective loss  $\alpha_{\text{eff}}$  as the product of overlap area and water absorption loss as  $\alpha_{\text{eff}} = \Gamma \alpha_{\text{water}}$ . Here  $\alpha_{\text{water}}$  is the absorption coefficient of water. The contaminant-limited  $Q$  factor ( $Q_{\text{cont}}$ ) can be expressed as:

$$Q_{\text{cont}} = \frac{2\pi n_{\text{eff}}}{\lambda \alpha_{\text{eff}}} \quad (5)$$

Figure 2h presents the simulation results, showing that the microcavity diameter varies from 0.1 mm to 3.0 mm, while the water layer thickness ranges from 0.1 nm to 10 nm. It is observed that the  $Q_0$  factor decreases exponentially with increasing water layer thickness. For the microcavity with a diameter of 3 mm discussed in this study and a water layer thickness of 1 nm, the  $Q_{\text{cont}}$  factor decreases from  $10^{10}$  level to  $10^9$  level. This finding indicates that even a slight reduction in the water layer's thickness results in a significant enhancement for  $Q$  factor, underscoring the primary inhibitory effect of contaminant loss on this parameter (see details in Supplementary Note S1.4). Finally, referring Eq. (1), meanwhile using the measured  $Q_{\text{abs}}$  and  $Q_{\text{sca}}$  data, we show the estimated  $Q_{\text{cont}}$  of the 10 microcavity samples in Fig. 2i. Typically,  $Q_{\text{cont}}$  of a silica micro-rod is on  $10^8$ - $10^9$  level, and there is a significant variance in the distribution.

Based on a detailed analysis of the composition and specific limitations of intracavity losses, now we can begin comprehensive

optimization efforts to enhance the intrinsic  $Q$  factor. First, we raise a method to polish the surface of the microrod. Figure 3a shows the SEM images during the process of polishing the surface of the microrod. In the left panel, we show the surface of the microrod before polishing, which exhibits obvious defects and non-uniformities. Utilizing a rough polishing process based on a carbon dioxide laser, the surface of the rod becomes smoother. However, due to the dust generated after the laser curing of silica, the tip area of the microcavity becomes covered with a large number of silica micro-nano particles, as shown in the middle panel. Then, we add a fine polishing process using a faster laser rotation speed with lower power. This step melts the tip area of the microcavity, achieving a very smooth surface, as shown in the right panel. During the fabrication process described above, surface roughness is also monitored using atomic force microscopy (AFM), as shown in Fig. 3b. Following rough polishing, the RMS roughness decreased from 11.2 nm to 0.73 nm. With subsequent fine polishing, the RMS roughness was further reduced to 0.46 nm, indicating that atomic-level smoothness has been achieved on the cavity surface. More detailed measurements are shown in Supplementary Note S3.3.

After two-step polishing process,  $Q_{\text{sca}}$  approaches  $2.2 \times 10^{11}$ . As shown in the left panel of Fig. 3c, measured intrinsic  $Q$  factor ( $Q_0$ ) in this case reaches  $1.05 \times 10^9$ . At this point, radiation and scattering losses are much lower than absorption losses, while contaminant loss becomes the dominant limitation. Specifically, assuming no contamination-induced loss on the microcavity, the intrinsic  $Q$  factor ( $Q_0$ ) should approach  $1.2 \times 10^{10}$ . Then, to reduce contaminant loss and improve the intrinsic  $Q$  factor, we heat the microcavity to evaporate the water layer and then fill it with nitrogen ( $\text{N}_2$ ) to seal it, thereby isolating it from water vapor. After the heating process, the water layer on the surface is temporarily eliminated. The middle panel of Fig. 3c presents the evolution curve of the intrinsic  $Q$  factor during this operation (see details in Supplementary Note S3.2). During the heating and  $\text{N}_2$  supply stages, the water vapor on the microcavity surface is gradually evaporated and removed by the  $\text{N}_2$ . As the microcavity cools down while continuing to be exposed to  $\text{N}_2$ , re-adsorption of water vapor is prevented. Consequently, the intrinsic  $Q$  factor stabilizes over  $8 \times 10^9$ . In the right panel of Fig. 3c, we demonstrate a standard case, where we obtain an intrinsic  $Q$  factor  $8.28 \times 10^9$ . When the  $\text{N}_2$  supply is stopped, the presence of hydroxyl groups on the cavity surface causes a minor re-absorption of water molecules from the atmosphere, leading to a slight decrease in the  $Q$  factor. However,  $Q_0$  remains stable at about  $7 \times 10^9$ . At this point, the microcavity can be encapsulated in an airtight device (Fig. 3d) for subsequent out-of-laboratory applications.

Figures 3e and 3f illustrate the results of repeated tests on the  $Q_0$  improvement and the loss components from 10 samples. According to Eq. (1) and the results from the loss analysis, the proportions of various losses in the microcavity in its original state, after polishing, and after heating are summarized in Fig. 3e. Here the data is averaged in 10 microcavity samples. Initially, in the original state, the proportions of absorption loss, scattering & radiation loss, and contaminant loss are 0.3%, 96.2%, and 3.5%, respectively, with scattering being the major limiting factor. After polishing, these proportions change to 8.3%, 0.5%, and 91.2%, respectively, with contaminant loss becoming the most significant factor. Following heating, the proportions shift to 65.8% for absorption loss, 3.7% for scattering & radiation loss, and 30.5% for contaminant loss, making absorption loss the primary limiting factor. As shown in Fig. 3f, in average, the polishing technique increases the original  $Q_0$  from  $4.5 \times 10^7$  to  $1.05 \times 10^9$ , and subsequent heating further improves it to  $8.28 \times 10^9$ , showing an enhancement of more than two orders of magnitude. This progression is significant evidence that the  $Q$  factor of our microcavity is approaching its theoretical limit, which is mainly determined by the material absorption. This technical scheme offers excellent scalability. In Supplementary Note S3.3, we also significantly improve the  $Q_0$  of silica microsphere,



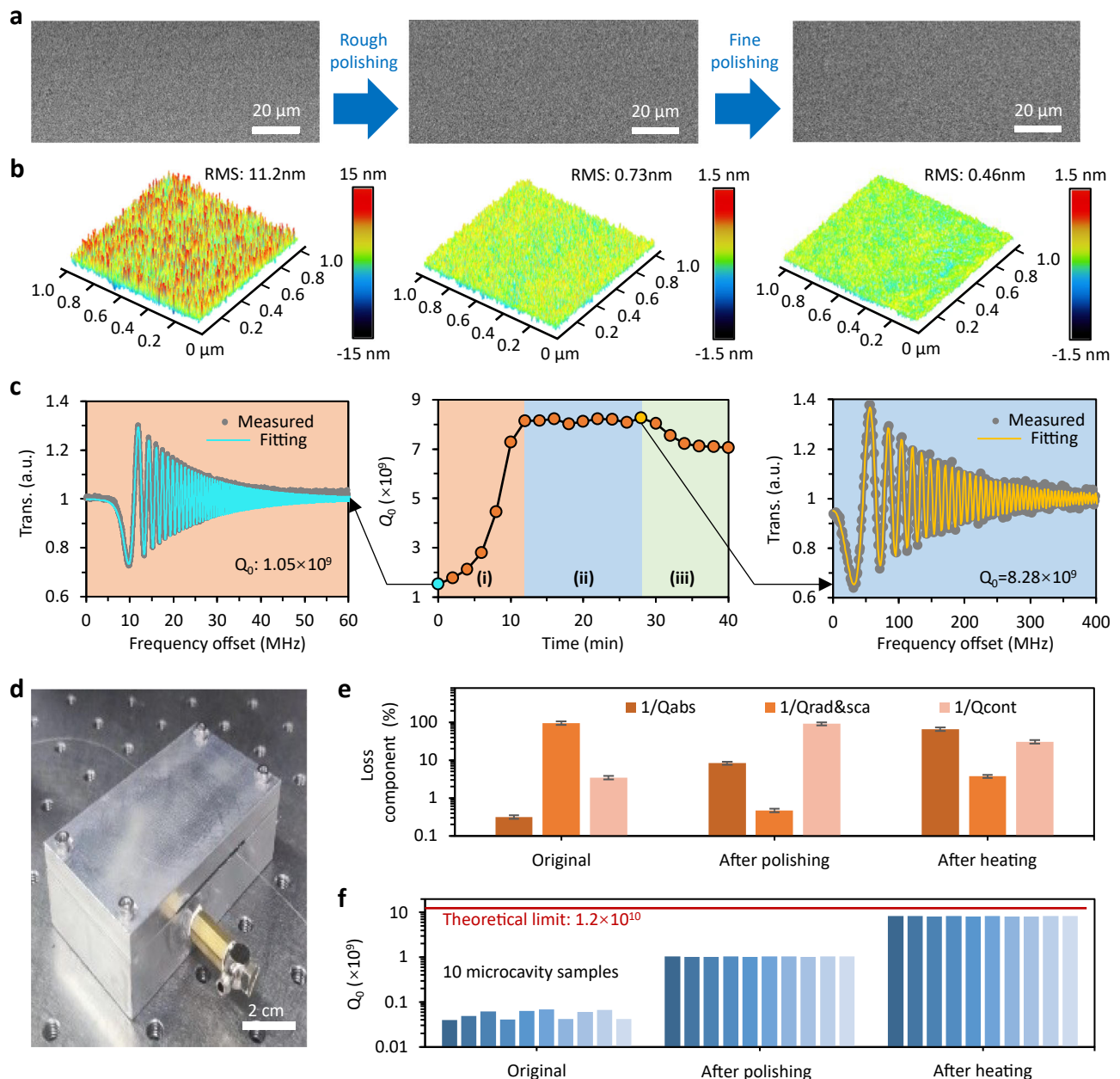


**Fig. 3 | Boosting the  $Q_0$  via fine-polishing and heating.** **a** Scanning electron microscope (SEM) images of microcavity surface. **b** Atomic force microscope (AFM) images show a root-mean-square (RMS) roughness of 0.46 nm, and a surface inhomogeneity coefficient of 7.84 nm, after the fine polishing process. **c** Left: Ringdown curve of the microcavity after two-step polishing. Middle: The  $Q_0$  evolution during the heating, stable and recovery process. Right: Measured ringdown curve after heating process, showing that the intrinsic  $Q$  factor of the microcavity

could be finally increased to  $8.28 \times 10^9$ . **d** Picture of the encapsulated device after heating, microrod inside keeps its  $Q_0$  higher than  $7 \times 10^9$  level. **e** The proportions of various losses in the original, polished, and heated microcavity, respectively. Error bars: uncertainty in repeated measurements for 10 microcavity samples. **f** Improvement of the intrinsic  $Q$  factor from the original state to the final state after polishing and heating, here we record 10 microcavity samples.

silica microtoroid and  $\text{MgF}_2$  cavities by implementing the two-stage laser polishing & in- $\text{N}_2$  heating.

## Discussion

In various applications, the realization of an ultrahigh- $Q$  microcavity is of significant importance. For instance, a high- $Q$  microcavity can be utilized to stabilize optical laser sources, such as frequency combs, for frequency synchronization<sup>49,61</sup>. In this work, we demonstrate an example where we use this packaged high- $Q$  microrod to fully stabilize a Kerr soliton microcomb on-chip. Achieving full stabilization of a microcomb within a compact size is

challenging due to the difficulty in finding a miniature ultrastable optical frequency reference. However, with our microrod achieving a  $Q_0$  level of  $8 \times 10^9$ , it presents a promising candidate as an optical reference for comb locking.

Utilizing this device, we developed a stabilization scheme that locks both the pump frequency and the repetition rate for a dissipative Kerr soliton microcomb with a 100 GHz repetition rate, such a high repetition rate is usually hard to measure directly. Our setup is illustrated in Fig. 4a, and its schematic operation is displayed in Fig. 4b. In the two-point locking process for soliton stabilization, we employ two resonances of the microrod: one is used to lock the

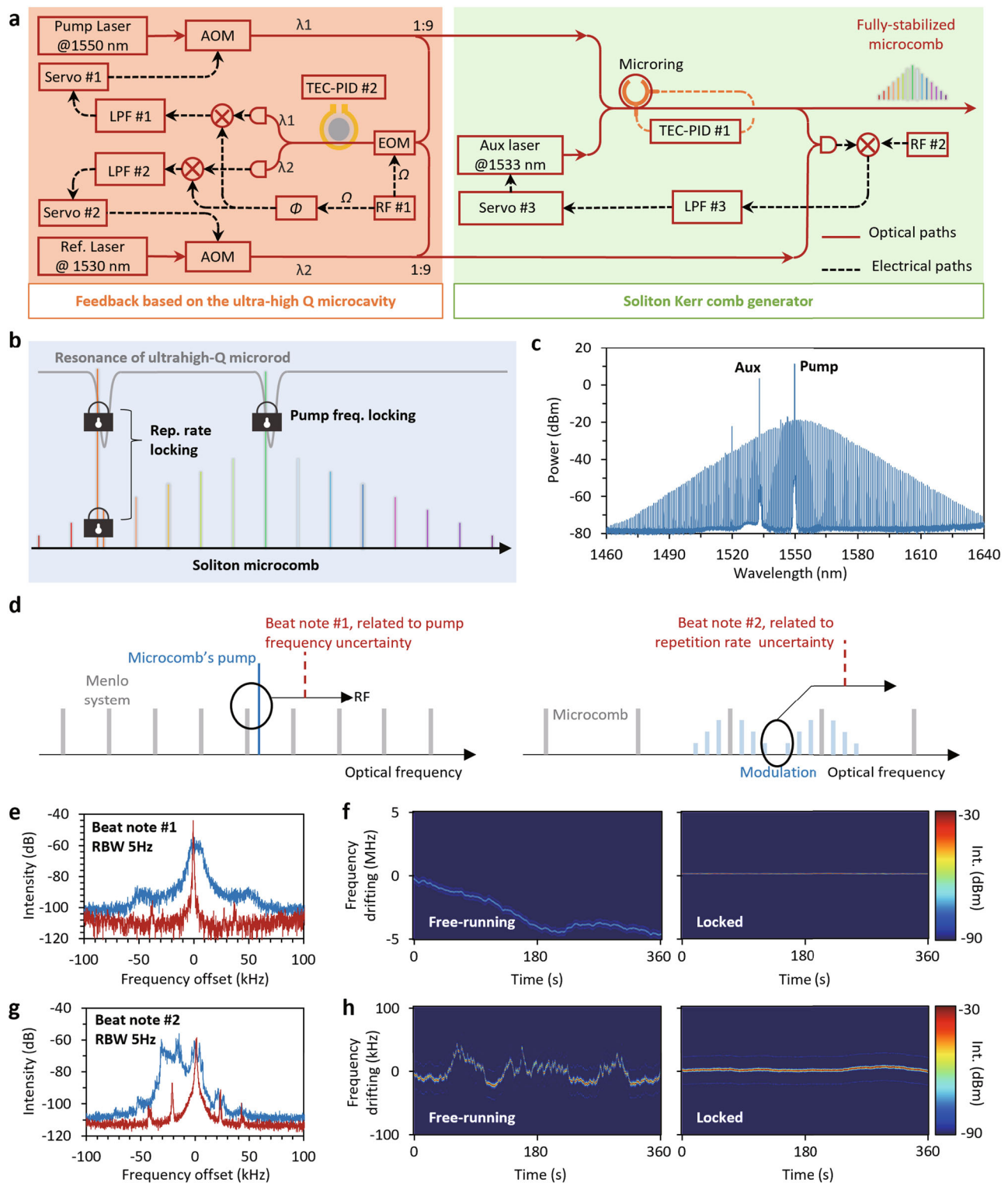


**Fig. 4 | Scheme for fully stabilizing an on-chip soliton microcomb utilizing the ultra-high  $Q$  microrod cavity.** **a** System setup, there are two parts: one is the feedback module based on the microrod (orange), the other one is the soliton Kerr microcomb generator. **b** Full stabilization operation of the soliton microcomb, using the ultra-high  $Q$  microcavity. **c** Optical spectrum of the fully stabilized soliton microcomb, here we mark two peaks: the auxiliary laser, and the pump laser.

**d** Scheme for measuring the noise of the pump laser (left) and for measuring the noise of repetition rate (right). **e** Spectrum of the beat note #1, before (blue curve) and after (red curve) stabilization. **f** Long-term stability of the beat note #1. **g** Spectrum of the beat note #2, before (blue curve) and after (red curve) stabilization. **h** Long-term stability of the beat note #2.

pump frequency at a wavelength of 1549.708 nm, while the other locks a frequency comb line at approximately 1529.864 nm. Specifically, loaded  $Q$  factor of the microrod device is about 4 billion under near-critical coupling conditions, suggesting a sensitivity to

frequency drifting  $4.13 \times 10^{-5}/\text{Hz}$ . We engage a single-frequency laser (pump, 1549.708 nm) to excite the soliton comb on-chip and another single-frequency laser (reference, 1529.864 nm) to lock the comb line via heterodyne detection. The steps for locking the feedback of the

pump and reference lasers are as follows: First, the pump laser (NKT-E15@1550 nm) and the reference laser (NKT-E15@1530 nm) are each directed through an acousto-optic modulator, then split into two paths using a 90:10 coupler. Second, 10% of the modulated pump laser and reference laser is utilized for servo locking. Third, the Pound-Drever-Hall (PDH) technique is applied to stabilize the output light from the acousto-optic modulator (AOM) at the resonance peak of the microrod cavity, with the feedback signal being applied to the modulation frequency of the AOMs. This process ensures stabilization of both the pump and reference laser frequencies.

Then, we lock the comb line around 1529.864 nm to the stabilized reference laser via optoelectronic heterodyne, where feedback is applied to an auxiliary laser for controlling the microring's cavity length, which determines the repetition rate. The steps for locking the repetition rate are as follows: First, the remaining 90% of the modulated reference laser and the output soliton microcomb are simultaneously input into the photodetector, where the reference laser beats with the comb tooth that has the closest frequency. Second, the resulting beat signal is mixed with a microwave reference to produce an error signal. Finally, this error signal is fed into the servo, and the feedback signal is applied to the output power of the auxiliary laser to achieve stabilization of the repetition rate. More information on the experimental design can be found in Supplementary Note S3.3. In Fig. 4c, we present the spectrum of our fully stabilized soliton microcomb, marking the positions of the pump laser and auxiliary laser.

As shown in Fig. 4d, our experimental setup involves two key tests: 1) To accurately characterize the noise suppression effect on the pump frequency, a fully stabilized fiber laser frequency comb instrument (Menlo System FC 1500-ULNova-ORS) is employed as the calibrator; 2) To evaluate the noise suppression effect on the repetition rate, we modulate the microcomb lines and measure the down-converted signal. Here, beat note #1 reflects the uncertainty of the pump frequency, while beat note #2 indicates the uncertainty of the repetition rate. In Fig. 4e, we display the measured spectrum of beat note #1, both before and after stabilization. In free-running operation, beat note #1 exhibits an instantaneous 10 dB bandwidth of 13 kHz. After stabilization, this bandwidth is reduced to 400 Hz. Figure 4f illustrates the long-term stability of the pump frequency. Before stabilization, the pump frequency experiences drifts approaching 5 MHz over a period of 360 seconds. Once stabilized, it remains nearly constant at 0 MHz. Figure 4g presents the measured spectrum of beat note #2, both before and after stabilization. With stabilization, the instantaneous 10 dB bandwidth is significantly reduced from 40 kHz to 600 Hz. Figure 4h depicts the long-term stability of the repetition rate. Prior to stabilization, the repetition rate drift is  $\pm 30$  kHz over 360 seconds, whereas post-stabilization, its uncertainty is reduced to less than  $\pm 3$  kHz over the same period.

In Fig. 5, we discuss the stabilization performance. In Fig. 5a, the single sideband phase noise (SSB-PN) of the pump laser is presented. In free-running state, the SSB-PN is 68.8 dBc/Hz at a 1 Hz offset, while reaching  $-90$  dBc/Hz at a 1 MHz offset. When stabilized by our microrod high- $Q$  cavity, the SSB-PN reduces to 23.6 dBc/Hz at a 1 Hz offset, demonstrating a maximum phase noise suppression of 45.2 dB for the pump laser. In Fig. 5b, using the micro-rod as a reference, we achieve an SSB-PN of the repetition rate of 16.1 dBc/Hz at a 1 Hz frequency offset, demonstrating phase noise suppression exceeding 60.6 dB for the repetition rate. In comparison, other microcavities, such as a fiber F-P microcavity ( $Q = 1.4 \times 10^8$ ) and an on-chip silicon nitride micro-ring ( $Q = 5 \times 10^6$ ), do not demonstrate such a significant noise suppression effect. In both of these figures, the green line indicates the thermal noise floor ( $-90$  dBc/Hz).

In Fig. 5c and d, we present the measured Allan deviations. In a free-running state, the Allan deviation of the pump laser increases from  $7 \times 10^{-11}$  to  $5.6 \times 10^{-9}$  as the gating time extends from 100  $\mu$ s to 100 s. Meanwhile, the Allan deviation of the repetition rate remains above  $5.4 \times 10^{-11}$ . Notably, the Meno System exhibits the best long-term stability; however, it is large and costly. Utilizing our micro-rod cavity as the reference, for the stabilized soliton microcomb, the minimum Allan deviation of the pump laser and the repetition rate reach  $1.2 \times 10^{-13}$  and  $2.2 \times 10^{-13}$ , respectively. This performance surpasses that achieved with a fiber F-P microcavity ( $Q = 1.4 \times 10^8$ ) or an on-chip micro-ring ( $Q = 5 \times 10^6$ ), demonstrating that a microcavity with a higher  $Q$  factor holds greater potential for microcomb stabilization. Finally, in Figs. 5e–f, we summarize the instantaneous linewidths of the pump laser and the minimum one-second uncertainties for the comb lines. The instantaneous linewidth of the micro-rod stabilized pump laser reaches 1.5 Hz, which is comparable to the scheme using the Menlo System (0.9 Hz) and significantly smaller than other strategies. Meanwhile, the one-second uncertainty in the micro-rod stabilization is less than  $1.6 \times 10^{-13}$ , highlighting its superiority over locking schemes employing other microcavities with lower  $Q$  factors. Related discussion can be found in Supplementary Note S3.3.

In this article, we present a method for quantitatively analyzing and optimizing the intracavity quality factor, applying it experimentally to a silica micro-rod whispering-gallery-mode cavity. We systematically characterize intracavity losses from material absorption, radiation/scattering, and contaminants, and identify contaminant loss as a critical barrier to improving the intrinsic  $Q$  factor toward to the theoretical limit. By implementing laser-smoothing techniques, we reduce radiation/scattering loss from  $2.41 \times 10^{-8}$  to  $4.5 \times 10^{-12}$ , and using the in- $N_2$  heating strategy, we decrease contaminant loss from  $8.68 \times 10^{-10}$  to  $3.68 \times 10^{-11}$ . Consequently, we enhance the intrinsic  $Q$  factor of the microcavity from  $4 \times 10^7$  to  $8.28 \times 10^9$ . This ultra-high  $Q$  achievement positions the cavity as an excellent candidate for optical stabilization. Using the  $Q$ -enhanced microrod as a reference, we achieve a fully stabilized soliton Kerr microcomb. Experimentally, we demonstrate phase noise suppression exceeding 45.2 dB for the pump laser and over 60.6 dB for the repetition rate. This work fundamentally elucidates the detailed loss components in a silica microcavity, provides a practical approach to achieving microresonators with exceptionally high  $Q$ , and highlights their potential as practical devices. Our results and discussions not only deepen the understanding of optical loss but also offer inspiration for microcavity-based applications.

## Methods

### Measurement of $Q$ factors

A tunable narrow linewidth laser at 1550 nm is coupled into the microcavity via a tapered fiber. The typical diameter of the tapered fiber is  $\sim 2$   $\mu$ m, and it is attached to the microcavity surface for stable and efficient coupling (coupling efficiency as high as  $\sim 96\%$ ). The frequency of the laser is scanned at a speed of 1 nm/s and calibrated by a Mach-Zehnder interferometer (MZI). The transmission spectrum is analyzed using a ringdown fitting model<sup>62</sup> (see details in Supplementary Note S1 & S3).

### Fabrication process of silica microrod cavity

The silica microrod cavity is fabricated in a fiber preform via laser machining technology. Firstly, a fused silica rod with a length of 4.5 cm is fixed on the rotating shaft via the clamp. Subsequently, the rotating fiber preform is processed by the focused laser controlled by the automatic program. Finally, the silica rod is

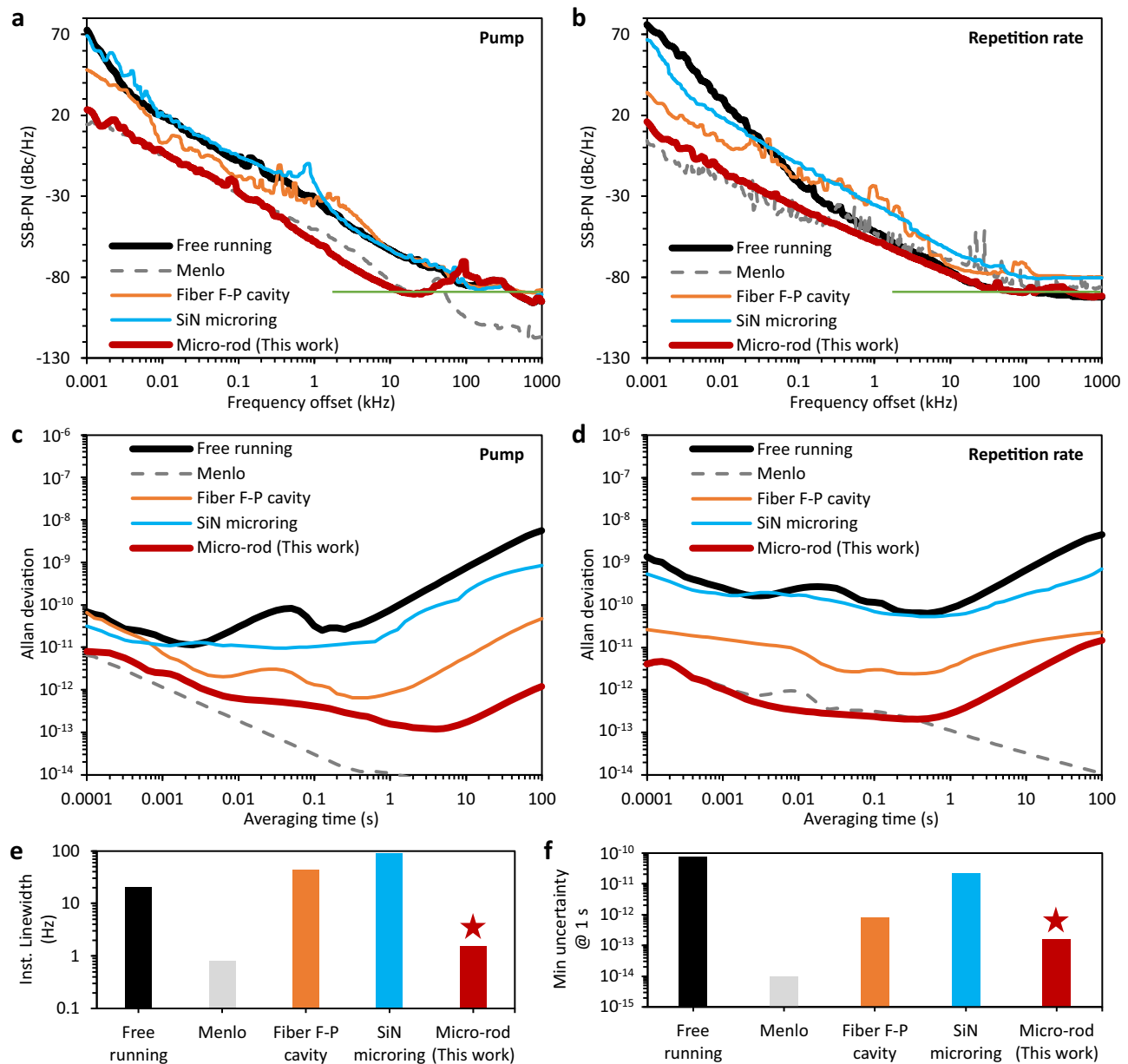


**Fig. 5 | Noise suppression performance.** **a** SSB-PNs of the pump laser. **b** SSB-PNs of the repetition rate. Here the green line marks the thermal noise floor. **c, d** Allan deviations, for the pump laser and the repetition rate. In above 4 panels, we

demonstrate the results using varied stabilization schemes. **e** Instantaneous linewidths. **f** Minimum uncertainties in 1 second. Here, performances of diverse stabilization strategies are compared.

annealed to reduce the surface roughness and control the edge curvature of the microrod cavity (see details in Supplementary Note S2).

### Packaging process of silica microrod cavity

The microrod cavity is securely housed within a custom-built aluminum enclosure, consisting of an inner and outer box connected with screws. The position of the tapered fiber is finely tuned via a precision three-dimensional nanopositioning platform to ensure optimal coupling. Once the optimal coupling position is achieved, a low-loss ultraviolet (UV) adhesive is applied to fix the microrod and tapered fiber. For temperature regulation, a 10 k $\Omega$  thermistor is placed within the enclosure, with a thermoelectric cooler (TEC) situated between the inner and outer boxes. In addition, a thermal tape is applied to the TEC to expedite heat transfer. Finally, the TEC is connected to the temperature controller via the lead and switchboard, and a PID controller is used to precisely control the temperature of the microrod cavity (see details in Supplementary Note S2).

### Fully stabilized soliton microcomb

For a high repetition rate microcomb, the frequency of each comb line can be expressed as  $f_n = f_p + n f_{\text{rep}}$ , where  $f_n$  represents the frequency of the comb line corresponding to the mode number  $n$ ,  $f_p$  represents the frequency of the pump laser, and  $f_{\text{rep}}$  represents the repetition rate. Therefore, if the frequency of the pump laser and  $n$ th comb line can be stabilized at the same time, the entire optical frequency comb tooth can be locked. Based on this principle, a fully stabilized soliton microcomb is realized by referencing the pump laser and the  $n$ -th comb line to the ultrahigh  $Q$  microrod (see details in Supplementary Note S3).

### Data availability

The data that support the plots within this paper are provided in the Supplementary Information/Source Data file. All raw data generated during the current study are available from the corresponding author upon request. Source data are provided with this paper.



## References

- Vahala, K. J. Optical microcavities. *Nature* **424**, 839–846 (2003).
- Liu, J. et al. Emerging material platforms for integrated microcavity photonics. *Sci. China Phys. Mech. Astron.* **65**, 104201 (2022).
- Grudinin, I. S. et al. Ultra high Q crystalline microcavities. *Opt. Commun.* **265**, 33–38 (2006).
- Jiang, X. et al. Chaos-assisted broadband momentum transformation in optical microresonators. *Science* (1979) **358**, 344–347 (2017).
- Zhang, X. et al. Symmetry-breaking-induced nonlinear optics at a microcavity surface. *Nat. Photonics* **13**, 21–24 (2019).
- Zhang, M. et al. Electronically programmable photonic molecule. *Nat. Photonics* **13**, 36–40 (2019).
- Xiang, C. et al. Laser soliton microcombs heterogeneously integrated on silicon. *Science* (1979) **373**, 99–103 (2021).
- Shu, H. et al. Microcomb-driven silicon photonic systems. *Nature* **605**, 457–463 (2022).
- Liu, Y. et al. A photonic integrated circuit-based erbium-doped amplifier. *Science* (1979) **376**, 1309–1313 (2022).
- Feng, H. et al. Ultra-high-linearity integrated lithium niobate electro-optic modulators. *Photonics Res.* **10**, 2366 (2022).
- Karabchevsky, A., Katiyi, A., Ang, A. S. & Hazan, A. On-chip nanophotonics and future challenges. *Nanophotonics* **9**, 3733–3753 (2020).
- Qin, C. et al. Electrically controllable laser frequency combs in graphene-fibre microresonators. *Light Sci. Appl.* **9**, 185 (2020).
- Lee, H. et al. Chemically etched ultrahigh-Q wedge-resonator on a silicon chip. *Nat. Photonics* **6**, 369–373 (2012).
- Wu, L. et al. Greater than one billion Q factor for on-chip microresonators. *Opt. Lett.* **45**, 5129 (2020).
- Tan, T. et al. Gain-assisted chiral soliton microcombs. *ArXiv* arXiv:2008.12510v1 (2020).
- Puckett, M. W. et al. 422 Million intrinsic quality factor planar integrated all-waveguide resonator with sub-MHz linewidth. *Nat. Commun.* **12**, 934 (2021).
- Shen, B. et al. Integrated turnkey soliton microcombs. *Nature* **582**, 365–369 (2020).
- Lukin, D. M. et al. 4H-silicon-carbide-on-insulator for integrated quantum and nonlinear photonics. *Nat. Photonics* **14**, 330–334 (2020).
- Wang, C. et al. High-Q microresonators on 4H-silicon-carbide-on-insulator platform for nonlinear photonics. *Light Sci. Appl.* **10**, 139 (2021).
- Gong, Z. et al. High-fidelity cavity soliton generation in crystalline AlN micro-ring resonators. *Opt. Lett.* **43**, 4366 (2018).
- Liu, X. et al. Integrated High-Q crystalline AlN microresonators for broadband Kerr and Raman Frequency Combs. *ACS Photonics* **5**, 1943–1950 (2018).
- Lin, J. et al. Fabrication of high-Q lithium niobate microresonators using femtosecond laser micromachining. *Sci. Rep.* **5**, 8072 (2015).
- Fang, Z. et al. Monolithic integration of a lithium niobate microresonator with a free-standing waveguide using femtosecond laser assisted ion beam writing. *Sci. Rep.* **7**, 45610 (2017).
- Qu, Z. et al. Fabrication of an ultra-high quality MgF<sub>2</sub> microresonator for a single soliton comb generation. *Opt. Express* **31**, 3005 (2023).
- Qu, M. et al. Dynamic process of soliton generation in CaF<sub>2</sub> crystalline whispering gallery mode resonators with negative TO effects. *Opt. Express* **32**, 42846 (2024).
- Chen, H.-J. et al. Chaos-assisted two-octave-spanning microcombs. *Nat. Commun.* **11**, 2336 (2020).
- Tan, T. et al. Multispecies and individual gas molecule detection using Stokes solitons in a graphene over-modal microresonator. *Nat. Commun.* **12**, 6716 (2021).
- Zhang, H. et al. Soliton Microcombs Multiplexing Using Intracavity-Stimulated Brillouin Lasers. *Phys. Rev. Lett.* **130**, 153802 (2023).
- Li, J.-T. et al. Coherently parallel fiber-optic distributed acoustic sensing using dual Kerr soliton microcombs. *Sci. Adv.* **10**, eadf8666 (2024).
- Li, J., Lee, H., Chen, T. & Vahala, K. J. Characterization of a high coherence, Brillouin microcavity laser on silicon. *Opt. Express* **20**, 20170 (2012).
- Santis, C. T., Steger, S. T., Vilenchik, Y., Vasilyev, A. & Yariv, A. High-coherence semiconductor lasers based on integral high-Q resonators in hybrid Si/III-V platforms. *Proc. Natl. Acad. Sci.* **111**, 2879–2884 (2014).
- Spolitis, S. et al. IM/DD WDM-PON communication system based on optical frequency comb generated in silica whispering gallery mode resonator. *IEEE Access* **9**, 66335–66345 (2021).
- Mazur, M. et al. High spectral efficiency coherent superchannel transmission with soliton microcombs. *J. Lightwave Technol.* **39**, 4367–4373 (2021).
- Geng, Y. et al. Coherent optical communications using coherence-cloned Kerr soliton microcombs. *Nat. Commun.* **13**, 1070 (2022).
- Riemensberger, J. et al. Massively parallel coherent laser ranging using a soliton microcomb. *Nature* **581**, 164–170 (2020).
- Chang, B. et al. Dispersive Fourier transform based dual-comb ranging. *Nat. Commun.* **15**, 4990 (2024).
- Qin, C. et al. Co-generation of orthogonal soliton pair in a monolithic fiber resonator with mechanical tunability. *Laser Photon Rev.* **17**, 2200662 (2023).
- Guo, Y. et al. Optical microcavities empowered biochemical sensing: status and prospects. *Adv. Devices Instrum.* **5**, 0441 (2024).
- Liang, Y. et al. Harnessing sub-comb dynamics in a graphene-sensitized microresonator for gas detection. *Front. Optoelectron.* **17**, 12 (2024).
- An, N. et al. Brillouin lasers in a graphene microresonator for multispecies and individual gas molecule detection. *APL Photonics* **8**, 100801 (2023).
- Guo, Y. et al. A monolithic graphene-functionalized microlaser for multispecies gas detection. *Adv. Mater.* **34**, 2207777 (2022).
- Zhang, L. et al. Ultrahigh-Q silicon racetrack resonators. *Photonics Res.* **8**, 684 (2020).
- Li, J., Suh, M.-G. & Vahala, K. Microresonator Brillouin gyroscope. *Optica* **4**, 346 (2017).
- Silver, J. M. et al. Nonlinear enhanced microresonator gyroscope. *Optica* **8**, 1219 (2021).
- Armani, A. M., Armani, D. K., Min, B., Vahala, K. J. & Spillane, S. M. Ultra-high-Q microcavity operation in H<sub>2</sub>O and D<sub>2</sub>O. *Appl. Phys. Lett.* **87**, 151118 (2005).
- Lin, G. et al. Dependence of quality factor on surface roughness in crystalline whispering-gallery mode resonators. *Opt. Lett.* **43**, 495 (2018).
- Pfeiffer, M. H. P. et al. Ultra-smooth silicon nitride waveguides based on the Damascene reflow process: fabrication and loss origins. *Optica* **5**, 884 (2018).
- Gao, M. et al. Probing material absorption and optical nonlinearity of integrated photonic materials. *Nat. Commun.* **13**, 3323 (2022).
- Yao, L. et al. Soliton microwave oscillators using oversized billion Q optical microresonators. *Optica* **9**, 561 (2022).
- Yang, K. Y. et al. Bridging ultrahigh-Q devices and photonic circuits. *Nat. Photonics* **12**, 297–302 (2018).
- Zhu, S. et al. All-optical controllable electromagnetically induced transparency in coupled silica microbottle cavities. *Nanophotonics* **7**, 1669–1677 (2018).

52. Cao, Y., Dai, J., Peng, X.-B., Ma, J.-Y. & Zhao, Q. Ultra-low threshold pH sensor based on a whispering gallery mode microbubble resonator. *Appl. Phys. Lett.* **124**, 244101 (2024).
53. Del'Haye, P., Diddams, S. A. & Papp, S. B. Laser-machined ultra-high-Q microrod resonators for nonlinear optics. *Appl. Phys. Lett.* **102**, 221119 (2013).
54. Niu, R. et al. Repetition rate tuning and locking of solitons in a microrod resonator. *Opt. Lett.* **49**, 570 (2024).
55. Ye, Z. et al. Foundry manufacturing of tight-confinement, dispersion-engineered, ultralow-loss silicon nitride photonic integrated circuits. *Photonics Res.* **11**, 558 (2023).
56. Song, Y., Zhu, X., Zuo, X., Huang, G. & Lončar, M. Stable gigahertz and mmWave-repetition-rate soliton microcombs on X-cut lithium niobate. *Optica* **12**, 693 (2025).
57. Liu, X. et al. Aluminum nitride nanophotonics for beyond-octave soliton microcomb generation and self-referencing. *Nat. Commun.* **12**, 5428 (2021).
58. *CRC Handbook of Chemistry and Physics*. (CRC Press). <https://doi.org/10.1201/9781315380476>. (2016).
59. Gorodetsky, M. L., Savchenkov, A. A. & Ilchenko, V. S. Ultimate Q of optical microsphere resonators. *Opt. Lett.* **21**, 453 (1996).
60. Wu, L. et al. Hydroxyl ion absorption in on-chip high-Q resonators. *Opt. Lett.* **48**, 3511 (2023).
61. Liu, K. et al. 36 Hz integral linewidth laser based on a photonic integrated 4.0 m coil resonator. *Optica* **9**, 770 (2022).
62. Liu, T. et al. Optical microcombs in whispering gallery mode crystalline resonators with dispersive intermode interactions. *Photonics Res.* **10**, 2866 (2022).

## Acknowledgements

The authors thank Prof. Cheng Wang, Prof. Chun-Hua Dong, Prof. Yun-Feng Xiao, Dr. Xiao-Chong Yu, Dr. Hao-Jing Chen, Prof. Yong Geng, and Dr. Chang Li for their helpful discussions. This work acknowledges support from National Key Research and Development Program of China (Grant 2023YFB2806200 (B.C.Y.)), National Natural Science Foundation of China (Grant 12474372 (D.Q.Y.), U24A20311 (B.C.Y.), 62305050 (T.T.), 62125103 (S.G.H.), 62220106002 (S.G.H.)), Natural Science Foundation of Beijing Municipality (Grant Z210004 (D.Q.Y.)), Guangdong Basic and Applied Basic Research Foundation (Grant 2024A1515011665 (T.T.)), State Key Laboratory of Information Photonics and Optical Communications (Grant IPOC2024ZR01 (D.Q.Y.)).

## Author contributions

T.-Y.P., T.T., B.D., B.C. contributed equally to this work. B.-C.Y., D.-Q.Y., and S.-G.H. led the research. T.-Y.P., T.T., B.D., B.C., and F.T. performed

the experiment. T.T., B.C., and Y.-J.H. contributed the theoretical analysis. T.-Y.P., B.D., and Y.-Z.Y. finished the device packaging. T.T., B.C., and F.T. contributed to the soliton microcomb stabilization. All authors processed and analyzed the results. B.-C.Y., T.T., T.-Y.P., D.-Q.Y., and S.-G.H. prepared the manuscript.

## Competing interests

The authors declare no competing interests.

## Additional information

**Supplementary information** The online version contains supplementary material available at <https://doi.org/10.1038/s41467-025-63954-6>.

**Correspondence** and requests for materials should be addressed to Shan-Guo Huang, Da-Quan Yang or Bai-Cheng Yao.

**Peer review information** *Nature Communications* thanks the anonymous reviewer(s) for their contribution to the peer review of this work. A peer review file is available.

**Reprints and permissions information** is available at <http://www.nature.com/reprints>

**Publisher's note** Springer Nature remains neutral with regard to jurisdictional claims in published maps and institutional affiliations.

**Open Access** This article is licensed under a Creative Commons Attribution-NonCommercial-NoDerivatives 4.0 International License, which permits any non-commercial use, sharing, distribution and reproduction in any medium or format, as long as you give appropriate credit to the original author(s) and the source, provide a link to the Creative Commons licence, and indicate if you modified the licensed material. You do not have permission under this licence to share adapted material derived from this article or parts of it. The images or other third party material in this article are included in the article's Creative Commons licence, unless indicated otherwise in a credit line to the material. If material is not included in the article's Creative Commons licence and your intended use is not permitted by statutory regulation or exceeds the permitted use, you will need to obtain permission directly from the copyright holder. To view a copy of this licence, visit <http://creativecommons.org/licenses/by-nc-nd/4.0/>.

© The Author(s) 2025